

**UCC Library and UCC researchers have made this item openly available.  
Please [let us know](#) how this has helped you. Thanks!**

<b>Title</b>	Programmable spectral interferometric microscopy
<b>Author(s)</b>	Riza, Nabeel A.; Bakker, Maarten; Bokhari, Amana
<b>Publication date</b>	2005-03-01
<b>Original citation</b>	Riza, N. A.; Bakker, M. and Bokhari, A. (2005) 'Programmable spectral interferometric microscopy', Review of Scientific Instruments, 76, 033107 (10 pp). doi: 10.1063/1.1866832
<b>Type of publication</b>	Article (peer-reviewed)
<b>Link to publisher's version</b>	<a href="https://aip.scitation.org/doi/10.1063/1.1866832">https://aip.scitation.org/doi/10.1063/1.1866832</a> <a href="http://dx.doi.org/10.1063/1.1866832">http://dx.doi.org/10.1063/1.1866832</a> Access to the full text of the published version may require a subscription.
<b>Rights</b>	© 2005 American Institute of Physics. This article may be downloaded for personal use only. Any other use requires prior permission of the author and AIP Publishing. The following article appeared in Rev. Sci. Instrum. 76, 033107 (2005), and may be found at <a href="https://doi.org/10.1063/1.1866832">https://doi.org/10.1063/1.1866832</a>
<b>Item downloaded from</b>	<a href="http://hdl.handle.net/10468/10254">http://hdl.handle.net/10468/10254</a>

Downloaded on 2021-11-27T12:14:47Z

# Programmable spectral interferometric microscopy

Cite as: Rev. Sci. Instrum. **76**, 033107 (2005); <https://doi.org/10.1063/1.1866832>

Submitted: 14 December 2004 . Accepted: 10 January 2005 . Published Online: 01 March 2005

Nabeel A. Riza, Maarten Bakker, and Amana Bokhari



View Online




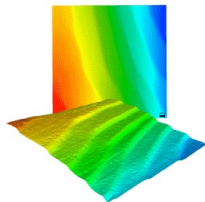
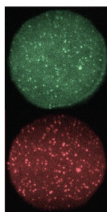


Export Citation

## ARTICLES YOU MAY BE INTERESTED IN

[External Raman standard for absolute intensity and concentration measurements](#)

Review of Scientific Instruments **76**, 033108 (2005); <https://doi.org/10.1063/1.1866952>

 <p><b>MCL</b> MAD CITY LABS INC. <a href="http://www.madcitylabs.com">www.madcitylabs.com</a></p>	<p>Nanopositioning Systems</p> 	<p>Modular Motion Control</p> 	<p>AFM and NSOM Instruments</p> 	<p>Single Molecule Microscopes</p> 
---	--	--	---	--

## Programmable spectral interferometric microscopy

Nabeel A. Riza,<sup>a)</sup> Maarten Bakker, and Amana Bokhari

*Nuonics, Inc., 1025 South Semoran Boulevard, Suite 1093, Winter Park, Florida 32792*

(Received 14 December 2004; accepted 10 January 2005; published online 1 March 2005)

A programmable optical sensor is proposed based on spectrally programmable heterodyne optical interferometric confocal microscopy implemented via an ultrastable in-line acousto-optic tunable filter (AOTF) based interferometer using double anisotropic acousto-optic Bragg diffraction. The design uses a tunable laser as the light source and anisotropic diffractions in an AOTF to generate two near-collinear orthogonal linear polarization and slightly displaced beams that both pass via the test sample to deliver highly sensitive sample birefringence or material optical retardation measurements. A spherical lens is used to form focused spots for high resolution confocal spatial sampling of the test object. Thus the instrument also forms a classic interferometric confocal microscope via the use of single mode fiber optics for the receive light. The laser and AOTF tuning allows birefringence measurements taken at different wavelengths, one at a time with minimal interwavelength crosstalk. Experimental demonstration of the instrument is achieved using a 1550 nm center 100 nm band tunable laser and variable birefringence liquid crystal and fixed retardance birefringent materials, all showing accurate retardation measurements to within a  $0.5^\circ$  rf phase accuracy. The instrument shows a fiber-in to fiber-out loss of 8.5 dB. An alternate design via a transmissive beam generation design provides collinear co-located beams on the sample plane for superaccurate measurements. © 2005 American Institute of Physics. [DOI: 10.1063/1.1866832]

### I. INTRODUCTION

It is well known that heterodyne optical interferometry can be used to detect very small changes in optical properties of a material, e.g., refractive index and material thickness. These changes can be manmade such as on a phase-encoded optical security card or environmentally induced such as by temperature changes in a jet engine. Material optical properties can also change due to chemical or biological perturbations. Heterodyne interferometry can also be used to take optical retardation or material birefringence measurements when using polarization interference microscopy where two orthogonal linear polarizations pass through a sample.<sup>1-5</sup> In addition, spectral interferometry is a useful measurement tool when sensing data is required for several independent wavelengths.<sup>6-9</sup> Acousto-optic deflectors (AOD) or Bragg cells using isotropic Bragg diffraction have been used to form Angstrom optical path length change sensitivity scanning heterodyne interferometers.<sup>10</sup> These interferometers use the changing radio frequency (rf) of the AOD or isotropic Bragg cell drive to cause a one dimensional (1D) scanning beam. These interferometers perform optimally for a fixed design wavelength.

The goal of this paper is to show how the basic fixed wavelength Ref. 10 design can be modified to realize a heterodyne spectral interferometric confocal microscope that operates over a broad optical bandwidth using efficient transmit/receive fiberoptics.<sup>11</sup> There are numerous important

applications for such a high sensitivity sensor that include material birefringence measurements, biomedical imaging using Fourier transform (FT) spectral interferometry (or FT OCT: Optical Coherence Tomography), refractive index or optical path length change measurements for environmental sensing, and real-time noninvasive monitoring of biological and chemical structures. The paper begins with the instrument design description including the optical flow operations that allow a stable birefringent measurement. Next, a proof of concept instrument is built and tested in the laboratory using liquid crystals and fixed retardation plates as the test birefringent materials. Finally, discussed are issues related to accurate birefringence measurements with this instrument.

### II. SPECTRALLY PROGRAMMABLE HETERODYNE OPTICAL INTERFEROMETRIC CONFOCAL MICROSCOPE DESIGN

Figure 1 shows the design of the spectrally programmable heterodyne optical interferometric confocal microscope using transmit/receive fiberoptics. Light from a fiber-coupled tunable laser passes through a fiber optic polarization controller (PC) to enter a 3-port fiber optic circulator C that feeds a single mode fiber (SMF) coupled fiber lens (FL) that produces a collimated laser beam in freespace. The PC is tuned so that this freespace laser beam is  $p$ -polarized (or horizontal or  $x$ -direction polarized). This  $p$ -polarized beam passes via a high extinction ratio polarizer  $P$  aligned to let  $p$ -polarization pass. This  $p$ -polarized light enters an AOTF

<sup>a)</sup>Electronic mail: nriza@aol.com

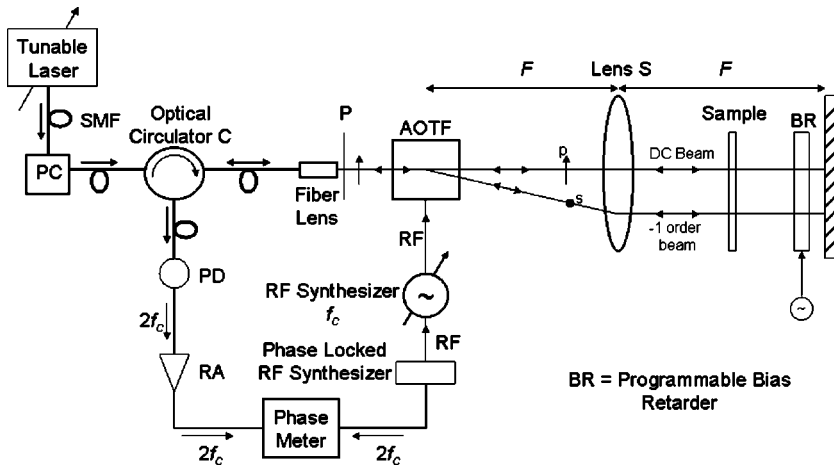


FIG. 1. Proposed design of the spectrally programmable heterodyne optical interferometric confocal microscope using transmit/receive fiber optics. The birefringent sample must be equivalent to being sandwiched between two parallel optically transmissive plates (e.g., glass plates with a liquid crystal layer) between the locations of the two probing beams passing through the sample.

that is Bragg matched such that this  $p$ -polarized input light generates an  $s$ -polarized (vertical or  $y$ -direction polarization) negative Doppler shifted  $-1$  order diffracted beam. By controlling the rf drive power and frequency of the AOTF drive, the AOTF diffraction efficiency and diffraction wavelength is selected such as to match the tunable laser wavelength for transmit mode operations of the instrument. The undiffracted or dc light from the AOTF stays  $p$ -polarized and without a Doppler shift. The  $-1$  order light gets a Doppler equal to the rf drive frequency  $f_c$ . These two AOTF output near collinear orthogonal linear polarization beams are made collinear but spatially separated by a focusing lens  $S$  of focal length  $F$ . The bias retarder (BR) and reference mirror  $M$  are placed very near the focal plane of spherical lens  $S$  and  $M$ . The two beams form focused spots on this focal plane and hence act a point spatial functions to measure optical properties of the inserted sample between  $S$ . Note that the birefringent sample must be equivalent to being sandwiched between two parallel optically transmissive plates (e.g., glass plates with a liquid crystal layer) between the locations of the two probing beams passing through the sample. This is because both beams must suffer the same optical path lengths, except for the much smaller change in path lengths due to the material birefringence. Because the beams go through the sample twice, the eventual raw data measures twice the birefringence of the sample, producing a factor of 2 improved sensitivity instrument versus a transmissive only instrument.

Figure 2 shows the proposed instrument design coordi-

ates with respect to the optical fast axis (FA) of the sample retarder with an unknown birefringence. Here the FA is measured from the instrument  $x$ -axis and is given by the anti-clockwise measured positive angle  $\varphi$  and  $\Gamma$  is the retardation of the sample. If  $\Gamma$  is negative, the slow axis (SA) is horizontal (or  $x$ -direction) and the FA vertical (or  $y$ -direction). A polarized light beam with its  $x$  (or  $p$ ) and  $y$  (or  $s$ ) electric field components after one pass through the retardation plate is given by the vector:

$$\begin{bmatrix} E'_x \\ E'_y \end{bmatrix} = W(\varphi, \Gamma) \begin{bmatrix} E_x \\ E_y \end{bmatrix}, \quad (1)$$

where

$$W(\varphi, \Gamma) = \begin{bmatrix} \cos(-\varphi) & \sin(-\varphi) \\ -\sin(-\varphi) & \cos(-\varphi) \end{bmatrix} \times \begin{bmatrix} \exp(-i\Gamma/2) & 0 \\ 0 & \exp(i\Gamma/2) \end{bmatrix} \times \begin{bmatrix} \cos \varphi & \sin \varphi \\ -\sin \varphi & \cos \varphi \end{bmatrix}.$$

Because of the reflection of the probe beams from the mirror  $M$ , the instrument reference (dc) and signal ( $-1$  order) beams will pass twice through the sample, in effect giving twice the sample retardation that allows the retardation matrix to be rewritten as

$$W(\varphi, \Gamma) = \begin{bmatrix} \exp(-i\Gamma)\cos^2 \varphi + \exp(i\Gamma)\sin^2 \varphi & \exp(-i\Gamma)\cos \varphi \sin \varphi - \exp(i\Gamma)\cos \varphi \sin \varphi \\ \exp(-i\Gamma)\cos \varphi \sin \varphi - \exp(i\Gamma)\cos \varphi \sin \varphi & \exp(-i\Gamma)\sin^2 \varphi + \exp(i\Gamma)\cos^2 \varphi \end{bmatrix}. \quad (2)$$

The incoming beams into the sample in the proposed instrument in Fig. 1 are the horizontally or  $p$ -polarized (dc) beam written as the vector  $\begin{bmatrix} 1 \\ 0 \end{bmatrix}$ , and the vertically or  $s$ -polarized ( $-1$  order diffracted) beam written as the vector  $\begin{bmatrix} 0 \\ 1 \end{bmatrix}$ . So after the double pass through the sample, the dc or reference beam becomes the electric field vector:

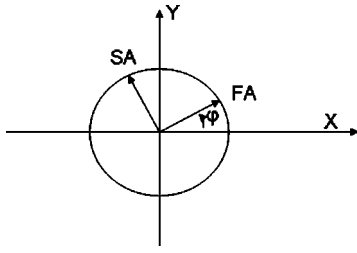


FIG. 2. Proposed instrument design coordinates with respect to the optical fast axis (FA) of the sample retarder with an unknown birefringence.

$$\begin{aligned}
 \begin{bmatrix} 1 \\ 0 \end{bmatrix} &\rightarrow \begin{bmatrix} E'_{x1} \\ E'_{y1} \end{bmatrix} \\
 &= W(\varphi, \Gamma) \begin{bmatrix} 1 \\ 0 \end{bmatrix} \\
 &= \begin{bmatrix} \exp(-i\Gamma)\cos^2\varphi + \exp(i\Gamma)\sin^2\varphi \\ \exp(-i\Gamma)\cos\varphi\sin\varphi - \exp(i\Gamma)\cos\varphi\sin\varphi \end{bmatrix}, \quad (3)
 \end{aligned}$$

while the  $-1$  order or Doppler shifted signal beam becomes the electric field vector:

$$\begin{aligned}
 \begin{bmatrix} 0 \\ 1 \end{bmatrix} &\rightarrow \begin{bmatrix} E'_{x2} \\ E'_{y2} \end{bmatrix} \\
 &= W(\varphi, \Gamma) \begin{bmatrix} 0 \\ 1 \end{bmatrix} \\
 &= \begin{bmatrix} \exp(-i\Gamma)\cos\varphi\sin\varphi - \exp(i\Gamma)\cos\varphi\sin\varphi \\ \exp(-i\Gamma)\sin^2\varphi + \exp(i\Gamma)\cos^2\varphi \end{bmatrix}. \quad (4)
 \end{aligned}$$

Note that the signal and reference beams now both contain both  $s$  (or  $y$ -direction) and  $p$  (or  $x$ -direction) polarization components. So far, this analysis assumes that the AOTF is driven for a 50:50 input light split such that 50% of input light is diffracted and the remaining 50% light stays in the dc or undiffracted beam. Note that by controlling the AOTF drive power, this split ratio can be optimized for a desired value. It is important to note that the AOTF only diffracts linearly polarized light if it is incident at the matching Bragg angle for this specific polarization. This condition in-turn has a unique effect for the returning  $-1$  order signal beam and the on-axis returning zero Doppler dc beam. Specifically, only the  $s$  component of the returning  $-1$  order is correctly Bragg matched with the AOTF and hence this  $s$ -component correctly undergoes Bragg diffraction that converted the input  $s$ -light to a  $p$ -polarized  $-1 \times -1$  double negative Doppler diffracted beam that is now on-axis with the original  $p$ -polarized input beam to the instrument. In effect, this  $-1 \times -1$  order  $p$ -polarized beam can enter the SMF fiber lens for transmission to the circulator  $C$  and then photodiode diode (PD) for eventual heterodyne detection with the returning reference beam. Hence, the returning  $p$ -polarized signal  $-1 \times -1$  order beam entering the fiber lens can be written as the electric field with only one component, namely the  $p$ -polarized component given by

$$E1x = \sqrt{a1}\{\exp(-i\Gamma)\sin^2\varphi + \exp(i\Gamma)\cos^2\varphi\}. \quad (5)$$

The diffraction efficiency for the AOTF for this second diffraction pass is assumed as  $a1$ . Note that the undiffracted  $\sqrt{(1-a1)}$  part of the  $s$ -polarized  $-1$  order beam component passes as  $s$ -polarized light through the AOTF (right to left in Fig. 1) and becomes off-axis (due to angular displacement) with the fiber lens position and hence does not enter the fiber lens and thus the PD. Moreover, the polarizer  $P$  between the AOTF and fiber lens FL will also block this return off-axis  $s$ -polarized light.

For the case of the returning on-axis reference dc beam with no Dopplers, both  $p$  and  $s$  components of this returning beam traveling right to left in Fig. 1 get to stay on-axis before the AOTF. The key point to note is that in this case, only the  $p$ -component of the returning beam is Bragg matched for AOTF diffraction; thus this  $p$ -component undergoes some Bragg diffraction (factor of  $\sqrt{a1}$ ) and polarization switching to  $s$ -polarized light. Since this new  $s$ -polarized light is angularly displaced and off-axis, and hence it will not enter the fiber lens and SMF. In addition, the polarizer  $P$  will block this  $s$ -light. The remaining  $\sqrt{(1-a1)}$  factor  $p$ -polarized reference zero Doppler beam light stays on axis and enters the fiber lens after passing through the polarizer. Hence, this returning on-axis  $p$ -polarized component of the reference zero Doppler beam entering the fiber lens can be written as

$$E2x = \sqrt{(1-a1)}\{\exp(-i\Gamma)\cos^2\varphi + \exp(i\Gamma)\sin^2\varphi\}. \quad (6)$$

On the other hand, the  $s$ -polarized component of the returning zero Doppler reference beam is not Bragg matched to the AOTF for  $s$ -polarized input beam diffraction. Hence this returning  $s$ -polarized zero Doppler reference beam component suffers no AOTF diffraction. Nevertheless, this  $s$ -polarized light traveling from right to left into the AOTF gets laterally translated due to the anisotropic nature of the AOTF crystal material (much like via a Calcite Beam Displacing Prism:BDP). In effect, this unwanted  $s$ -polarized returning beam gets laterally displaced with respect to the input light axis, and hence cannot enter the on-axis SMF or photodetector (PD). The AOTF design via its crystal dimensions is such that this unwanted  $s$ -polarized light is displaced such that it will completely miss the aperture of the fiber lens. Typically, this displacement is several millimeters (e.g.,  $>3$  mm) with a typical fiber lens diameter of 1.8 mm. Thus, even if no polarizer  $P$  is placed between fiber lens and AOTF in the Fig. 1 design, this unwanted  $E2y$  optical field does not enter the fiber optics and hence the PD, as the single mode fiber optics acts as a spatial filter that blocks the unwanted light. Another way to block this light is via pinhole-type spatial filters such as used in a freespace design embodiment of the proposed instrument. If the polarizer  $P$  is used in the proposed instrument design (Fig. 1), this  $E2y$  component which is  $s$ -polarized cannot pass via  $P$  into the fiber lens, making  $E2y=0$ . In addition, all other returning  $s$ -light is blocked by  $P$ . Note that because of space constraints, Fig. 1 does not show the displaced returning  $s$ -polarized beam that is traveling side-by-side with the on-axis  $p$ -beams. Typical angular beam displacement angles between the on-axis and diffracted beams for AOTF range in the  $1^\circ$ – $6^\circ$  range. Thus, the only

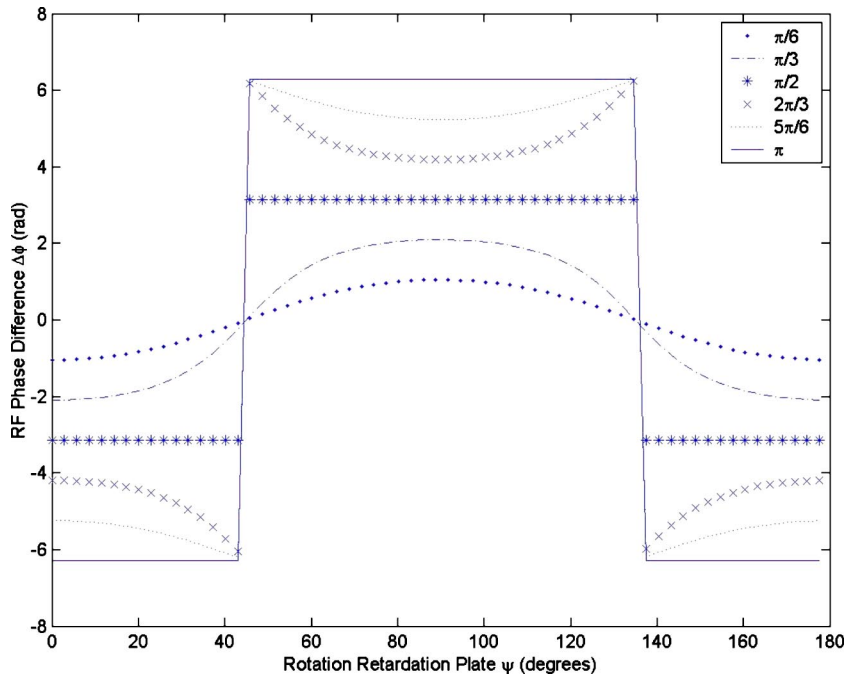


FIG. 3. Computer calculated plots of the proposed instrument rf phase difference in radians for various retardation values (e.g.,  $\pi/6$ ,  $\pi/3$ ,  $\pi/2$ ,  $2\pi/3$ ,  $5\pi/6$ , and  $\pi$ ) of a birefringent sample at various rotation angles of the sample FA.

beams that are also p-polarized, that eventually enter the fiber lens (or reach the PD) are the

- (a) zero Doppler reference beam given by  $E2x=E_2$  and the
- (b)  $2f_c$  Doppler shifted signal beam given by  $E1x=E_1$ , where  $f_c$  is the AOTF rf frequency.

This signal and reference beam pair travels via the circulator to the PD. The measured interferometric signal at a rf frequency  $2f_c$  generated by the photodetector PD is given by the expression:  $2|E_1||E_2|\cos(\phi_1-\phi_2)$ , where  $\phi_1$  and  $\phi_2$  are the phase values of the complex optical field components  $E_1$  and  $E_2$ , respectively. The relative rf phase shift from the optical instrument is generated by using external phased locked rf synthesized signal generators that produce an ex-

ternal rf reference signal at  $2f_c$  frequency that is fed to a lock-in amplifier/phase meter (PM) along with the  $2f_c$  rf signal generated by the PD. AOTF drive frequency signal at  $f_c$  is also generated by a phase-locked rf synthesizer. By observing and measuring both the amplitude and phase shift of the rf signal produced by the PD for a given sample location and sample rotational position with respect to the instrument  $x$  (or  $p$ ) and  $y(s)$  axes (see Fig. 2), one can deduce the retardance value and hence birefringence of the sample.

Using the previously stated expressions for  $E_1$  and  $E_2$ , the computed rf phase difference (Fig. 3)  $\Delta\phi=\phi_1-\phi_2$  obtained via the photodetector PD and the rf amplitude (Fig. 4) measured by the photodetector given as  $A=2$  times magnitude of  $E_1$  times magnitude of  $E_2$  are computer calculated.

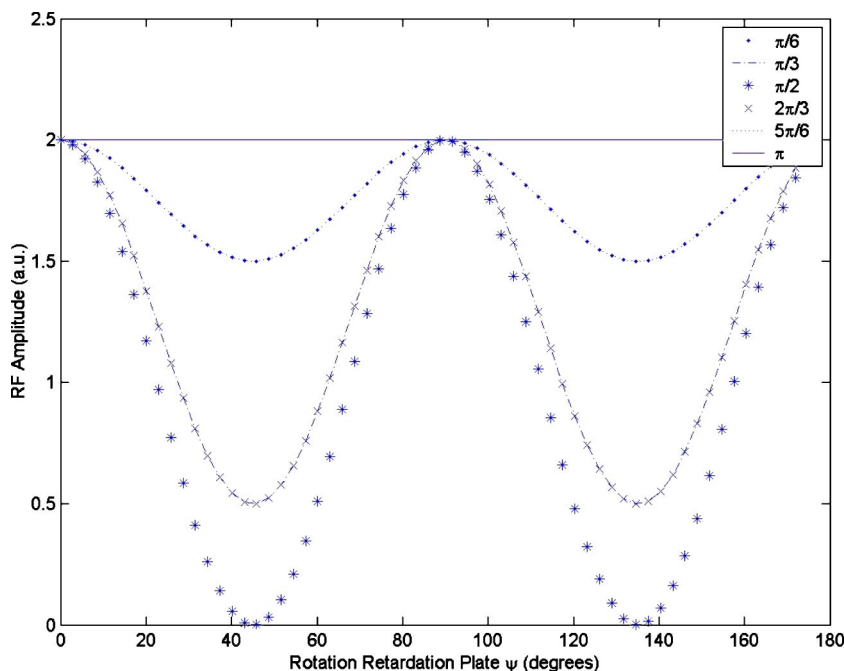


FIG. 4. Computer calculated plots of the proposed instrument output PD generated ac signal rf amplitude for various retardation values (e.g.,  $\pi/6$ ,  $\pi/3$ ,  $\pi/2$ ,  $2\pi/3$ ,  $5\pi/6$ , and  $\pi$ ) of a birefringent sample at various rotation angles of the sample FA.

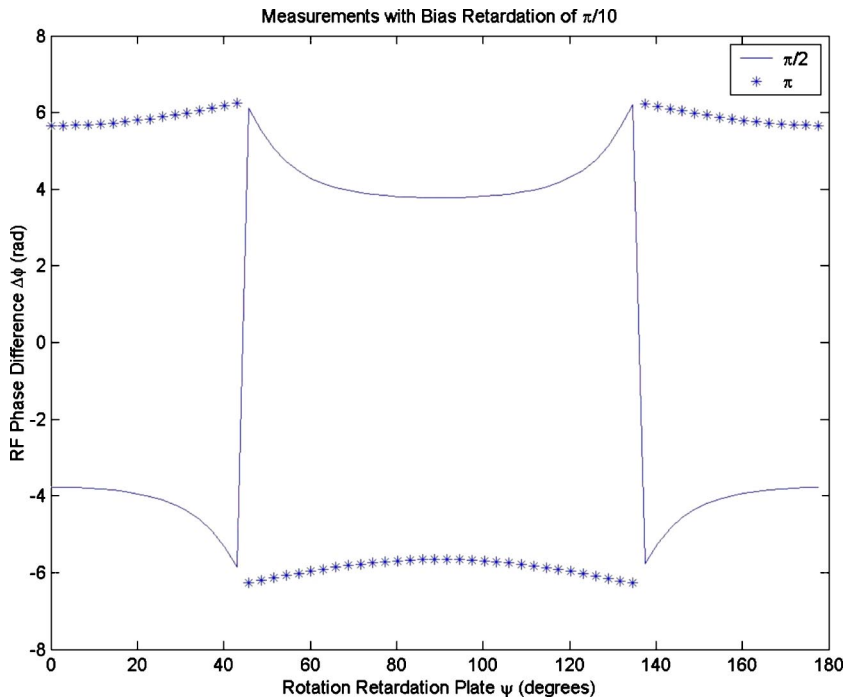


FIG. 5. Computer calculated plots of the proposed instrument output PD generated ac signal rf amplitude with an added  $\pi/10$  reference retardation bias for the ambiguous retardation values of  $\pi/2$  and  $\pi$  of a birefringent sample at various rotation angles of the sample FA.

The phase difference (Fig. 3) in radians is calculated for various retardation values (e.g.,  $\pi/6$ ,  $\pi/3$ ,  $\pi/2$ ,  $2\pi/3$ ,  $5\pi/6$ , and  $\pi$ ) of a birefringent sample at various rotation angles  $\psi$  of the sample FA. Similarly, the amplitude of the rf signal is calculated and plotted for various retardation values (e.g.,  $\pi/6$ ,  $\pi/3$ ,  $\pi/2$ ,  $2\pi/3$ ,  $5\pi/6$ , and  $\pi$ ) of a birefringent sample. These plots indicate the procedure to be used when calculating the birefringence for a given sample placed in the proposed instruments. This procedure is also used in the experimental section later in the paper. From the Fig. 4 amplitude signal plot, it is clear that when the sample is rotated through  $180^\circ$ , the rf signal minima occur at two FA rotation angles of angle  $\psi=45^\circ$  and  $\psi=135^\circ$ . The only case this is not

true is for the integer multiples of  $\pi/2$  retardation cases, where we will have to introduce a known bias retardation offset via the programmable bias retardation (PB) device in Fig. 1. The BR can be a parallel-rub nematic liquid crystal (NLC) electrically controlled phase cell where easily 0 to  $N\pi$  retardations (e.g.,  $N=5$ ) can be electrically introduced to remove measurement ambiguity when the mentioned rf amplitude minima ambiguity occurs or when high orders of sample retardation ( $>\pi$ ) are present. The BR is inserted with its FA (or SA) to align with the instrument  $x$  (or  $y$ ) axis or the other way around. Figures 5 and 6 show how the rf phase and rf amplitude plots change when a bias retardation is added for the original ambiguous cases of  $\pi/2$  and  $\pi$  retar-

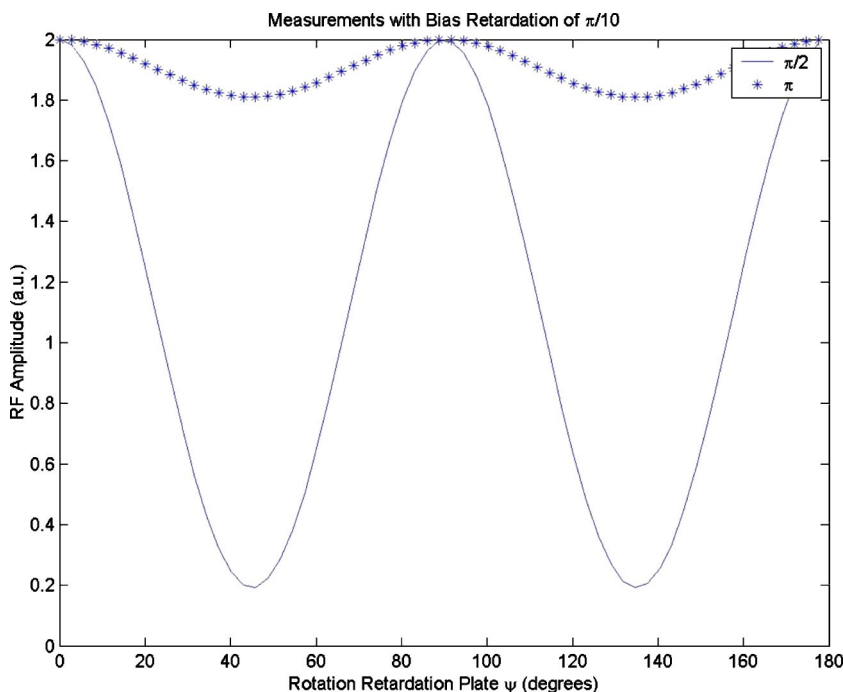


FIG. 6. Computer calculated plots of the proposed instrument rf signal phase difference with an added  $\pi/10$  reference retardation bias for the ambiguous retardation values of  $\pi/2$  and  $\pi$  of a birefringent sample at various rotation angles of the sample FA.

dation values, thereby again generating the two minima. Once the minima are known, then the sample FA or the SA location is known as it is  $45^\circ$  from these minima angles. At this rotation location where now the sample FA or SA is aligned with the instrument  $x$  (or  $y$ ) axis, the rf phase shift is experimentally measured as the sample retardance in degrees or radians. Since the wavelength  $\lambda$  is known, the sample retardance  $R$  can be converted to sample retardation in units of length (i.e., nanometers). Birefringence has units of retardation per unit path length of light, i.e., nanometer/centimeter. As the birefringent sample thickness  $d$  is known, the sample birefringence  $\Delta n$  can be calculated, as rf phase shift  $= (2\pi/\lambda) \Delta n d$ , where  $\Delta n d$  is the retardance  $R$ . To know which  $\psi$  angle or minima location marks the FA (or SA) of the sample, one must observe the phase data around the expected ( $45^\circ$  offset from the minima angle location) to see if the phase is increasing or decreasing and match it to the Fig. 3 plot. Depending on which phase change effect happens, the chosen test axis location can be labeled as the sample FA or SA. Thus, the proposed instruments can successfully determine the given birefringent sample's retardation and direction of FA and SA. As the instrument is calibrated, one can also access the transmission efficiency of the material by measuring the amplitude of the rf signal. Because the FA/SA of the BR is known, one can also measure the sign of the retardation for cases of large retardation ( $>\pi$ ). Fixed known value retardation plates can also be effectively used as fixed bias offsets instead of the programmable BR if the sample retardations are known to avoid the ambiguous states of multiples of  $\pi/2$  retardation. FA means direction of the sample where refractive index is small so the speed of light is faster compared to the other orthogonal direction in the sample where the index is higher and hence speed of light is slower.

It is important to note that the proposed instrument can take data on a per wavelength basis across a specified band. In effect, it becomes a spectroscopy tool. The per wavelength data can also be Fourier transformed electronically to implement FT OCT. Wavelength scanning interferometry approaches can also yield additional data, such as when analyzing high order retardations. The light sources that can be used include the tunable laser, but others can also be used including fixed wavelength lasers or broadband lasers. Other nonlaser source options are also possible, but with system constraints such as related to SMFs and confocal optics. The light sources and the AOTF can also be temporally modulated (e.g., time gated) to implement new sample probing capabilities such as in two photon imaging and other fluorescence imaging techniques. Note that the AOTF is a narrow-band wavelength filter that can be tuned to let the chosen light wavelength (or wavelengths) onto the sample or into the PD. Also note that an anisotropic acousto-optic deflector or anisotropic AO material Bragg cell can also be used instead of the AOTF in the proposed design. In this case, the instrument wavelength band of operations is limited. Based on optical sources and AOTFs available, a broad spectrum of wavelengths can be covered from the ultraviolet (UV), visible, near infrared (IR) to far IR. Both noncollinear-type and collinear-type AOTFs can be used with the proposed instru-

ment. The proposed microscope can have a great impact in many applications ranging from biomedical optics to liquid crystal testing.

### III. EXPERIMENT

The proposed instrument design in Fig. 1 is set-up in the laboratory using a 1500–1600 nm tunable semiconductor laser, a TeO<sub>2</sub> AOTF, an  $F=15$  cm lens  $S$ , a 1550 nm band fiber-coupled high speed PD, and two phase-locked rf synthesizers. The AOTF is driven for 50% or 3-dB diffraction efficiency (or  $a_1=0.5$ ). The fiber lens produces a 0.44 mm  $1/e^2$  minimum Gaussian beam waist diameter at a distance of 6 cm from the fiber lens face. The fiber lens is of the self-imaging-type with its beam waist positioned within the AOTF to produce the self-imaging condition required for high efficiency fiber-to-freespace optical coupling.<sup>12</sup> The instrument fiber-in to fiber-out optical loss is measured at 8.5 dB that includes 6 dB AOTF diffraction loss, 1.4 dB circulator loss, and 1.1 dB loss due to freespace-fiber coupling and Fresnel losses from the various bulk optical components. The rf signal leaving the PD has a frequency of  $2f_c$  and contains the phase information from the sample. This signal then passes through a rf signal amplifier (RA) and is fed to one channel of an oscilloscope. The rf synthesizer driving the AOTF is phase-locked with another frequency synthesizer that produces the reference rf signal of  $2f_c$  that is fed to another channel of the oscilloscope that is used as a rf phase meter. These phase-locked rf signals show a phase accuracy of  $0.5^\circ$  that in-turn sets a limit to the material birefringence measurement accuracy. To test the instrument, a 6- $\mu\text{m}$ -thick parallel-rub nematic liquid-crystal (NLC) cell is used as a birefringent sample. The cell is placed such that the its nematic director is along the  $s$ -polarization (or  $Y$ -direction). A 1590 nm birefringence measurement wavelength is chosen using an AOTF rf drive of  $f_c=45.85$  MHz giving a heterodyne detected PD produced rf signal output of  $2f_c=91.7$  MHz. The rf phase of the PD produced rf signal when compared to the external rf reference signal provides the phase information required to measure the birefringence of the sample.

Figure 7 shows three oscilloscope pictures of the test experiment using the NLC material. The lower signal is the synthesizer reference signal and the upper signal is the heterodyne detected PD signal. In Fig. 7(a), the voltage applied to the NLC cell is 0.05 V and thus the cell birefringence is at a maximum. In Fig. 7(c), the cell voltage applied is 5.0 V, implying near zero cell birefringence as nearly all NLC molecular directors are aligned along the optical beam propagation direction. Figure 7(b) condition of 2.3 V cell voltage lies between these extremes giving a birefringence between the extreme values of Figs. 7(a) and 7(c). Thus by changing the voltage on the NLC cell, the Fig. 1 instrument can measure the change in NLC birefringence with voltage. It is important to note that when there is a reference value, e.g., 5.0 V NLC drive voltage gives zero cell birefringence, the range of the birefringence measurements can be extended. Figure 8 shows this principle by plotting NLC cell birefringence data measured by the instrument where it is



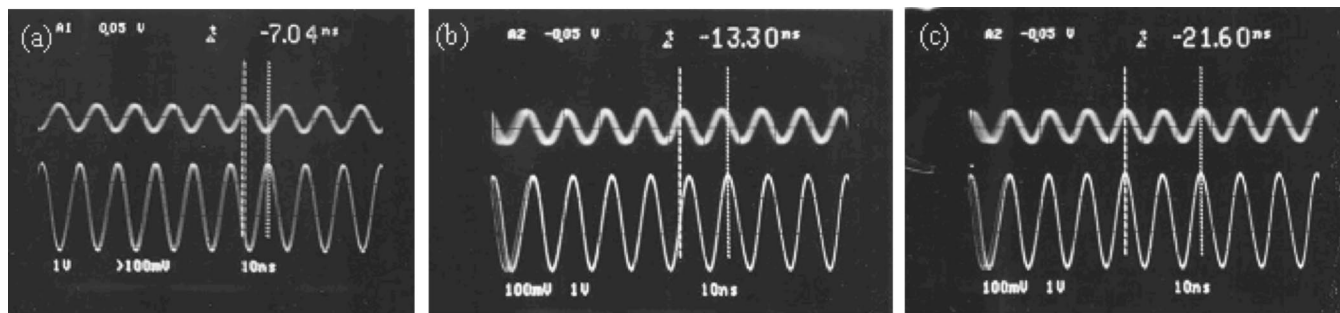


FIG. 7. Instrument provided rf phase shift experimental data for a NLC cell birefringent test sample. The wavelength used is 1590 nm. The NLC cell birefringence is electrically changed applying drives voltages of (a) 0.05 V, (b) 2.3 V, and (c) 5.0 V. Top traces from instrument and bottom traces from phase-locked synthesizer. Twice AOTF  $f_r=91.7$  MHz.

assumed that at 5.0 V NLC drive the NLC cell has no birefringence. Hence from this biasing point, the birefringence is calculated for different applied voltages  $V$  on the NLC cell using the expression:

$$\Delta\varphi = \left(\frac{2\pi}{\lambda_0}\right) |n_e(V) - n_o| d, \tag{7}$$

where  $\Delta\varphi$  is the rf relative phase measurement using the instrument,  $d=6 \mu\text{m}$  is the thickness of the NLC cell, and  $\Delta n = |n_e(V) - n_o|$  is the voltage  $V$  dependent NLC material birefringence. The assumption used is that when  $V=5$  V,  $|n_e(V) - n_o|$  is zero as also plotted in Fig. 8. For example if the voltage of the cell is such as to make  $\Delta\varphi = \pi/2$ , the NLC cell becomes a quarter-wave plate (QWP) or if  $\Delta\varphi = \pi$ , a half-wave plate (HWP) is realized.

Figure 9 shows how the proposed instrument provides material birefringence calculation data at different wavelengths, hence acting like a spectral microscope. The sample used is again the NLC cell, but this time there is no voltage applied on the NLC cell giving its maximum natural birefringence. The instrument is operated for three different wavelengths, i.e., Fig. 9(a) 1520 nm, (b) 1560 nm, and (c)

1600 nm. The  $f_c$  drive frequencies for the AOTF are Fig. 9(a) 48.1 ( $2f_c=96.2$ ) MHz, (b) 46.8 ( $2f_c=93.6$ ) MHz, and (c) 45.6 ( $2f_c=91.2$ ) MHz. The different rf phase shifts indicate the expected different NLC material birefringence for the three different test wavelengths.

Next the instrument is tested with a nonprogrammable fixed birefringence sample of a commercial standard Quarter Wave Plate (QWP) designed for 1550 nm. Because the linear polarized beams travel twice through the sample in the instrument, a total phase shift of  $\pi (= \pi/2 \times 2)$  exists between the interfering beams when they have passed the QWP sample implying that at 1550 nm, the instrument should show exactly a  $180^\circ$  rf phase shift. This experimental result is correctly proven by the instrument data shown in Figs. 10(c) and 10(d). Figure 10(c) data are without the QWP sample and Fig. 10(d) data are with the QWP inserted, thus indicating a rf phase shift of  $\pi$  between these pictures. Using the same instrument, the QWP birefringence is tested for two other wavelengths, i.e., 1520 nm in Fig. 10(a) and 10(b) and 1600 nm in Figs. 10(e) and 10(f). As expected, because the QWP is not designed for these wavelengths, other than a  $\pi$  RF phase shift is measured.

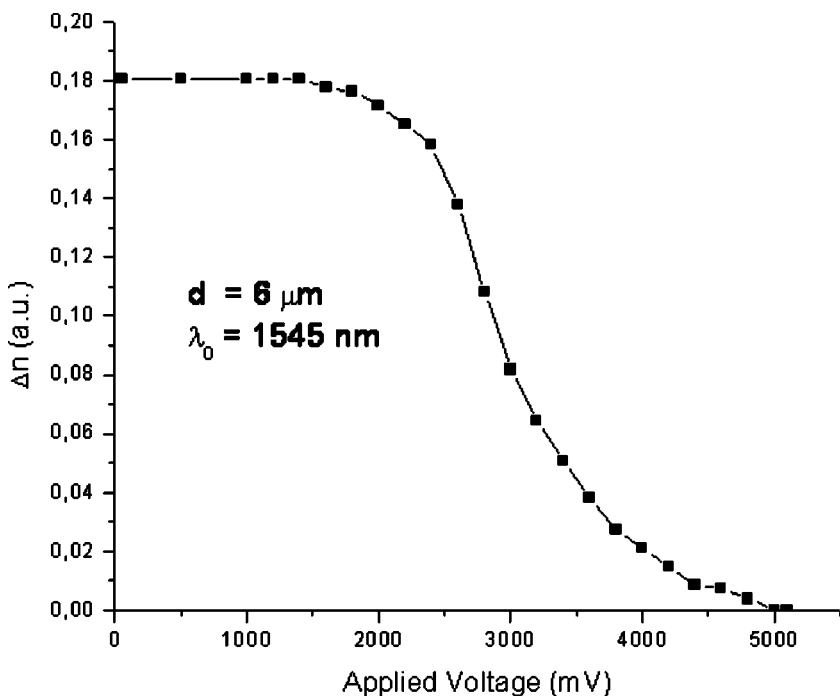


FIG. 8. Instrument measured NLC birefringence  $\Delta n$  at the tunable wavelength of 1545 nm as the applied voltage (mV) on the NLC cell is changed.

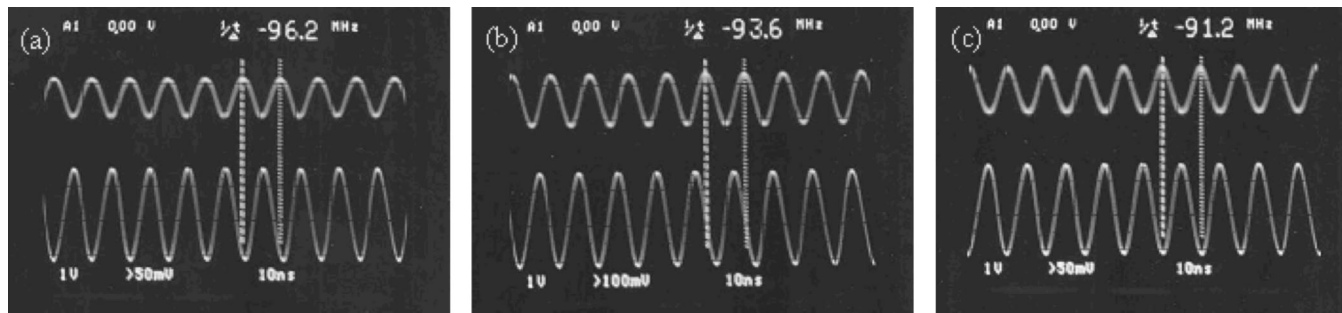


FIG. 9. Instrument provided rf phase shift produced with the NLC cell sample with no voltage applied and instrument wavelength tuned to (a) 1520 nm @ 96.2 MHz=2 X AOTF drive, (b) 1560 nm@ 93.6 MHz=2 X AOTF drive, and (c) 1600 nm@ 91.2 MHz=2 X AOTF drive. Top traces from instrument and bottom traces from phase-locked synthesizer.

When measuring optical birefringence, the orientation of the material fast axis (FA) or slow axis (SA) is desired. To find out how these axes are oriented, the test sample has to be rotated in the proposed instrument. This rotation operation (with respect to Fig. 2) for a birefringent material of unmarked FA/SA and different possible birefringence values is calculated mathematically and as mentioned before are shown in Figs. 3 and 4. In Fig. 3, the measured rf phase difference between the two linearly polarized beams probing the sample in the instrument is plotted against the rotation angle of the sample for different birefringence value retardation plates. As can be seen, only when the orientation of the

FA and SA are in line with the directions of the polarization of the two probing beams (i.e.,  $\psi=0$  or  $90^\circ$ ), the correct value for the retarder birefringence is measured. Recall that the instrument provides a rf phase measurement equivalent to twice the test sample retardation. For example, if a retarder with retardation of  $\pi/3$  is used as the test sample, the rf phase measured by the instrument should be  $\pm 2\pi/3$  radians or  $\pm 2.094$  on the y-axis scale of Fig. 3. Note that this rf phase condition is true when  $\psi$  is zero or  $90^\circ$ .

In Fig. 4 the amplitude of the measured rf signal is plotted against the rotation of the retardation plate showing that a maximum rf signal value occurs when the orientation of

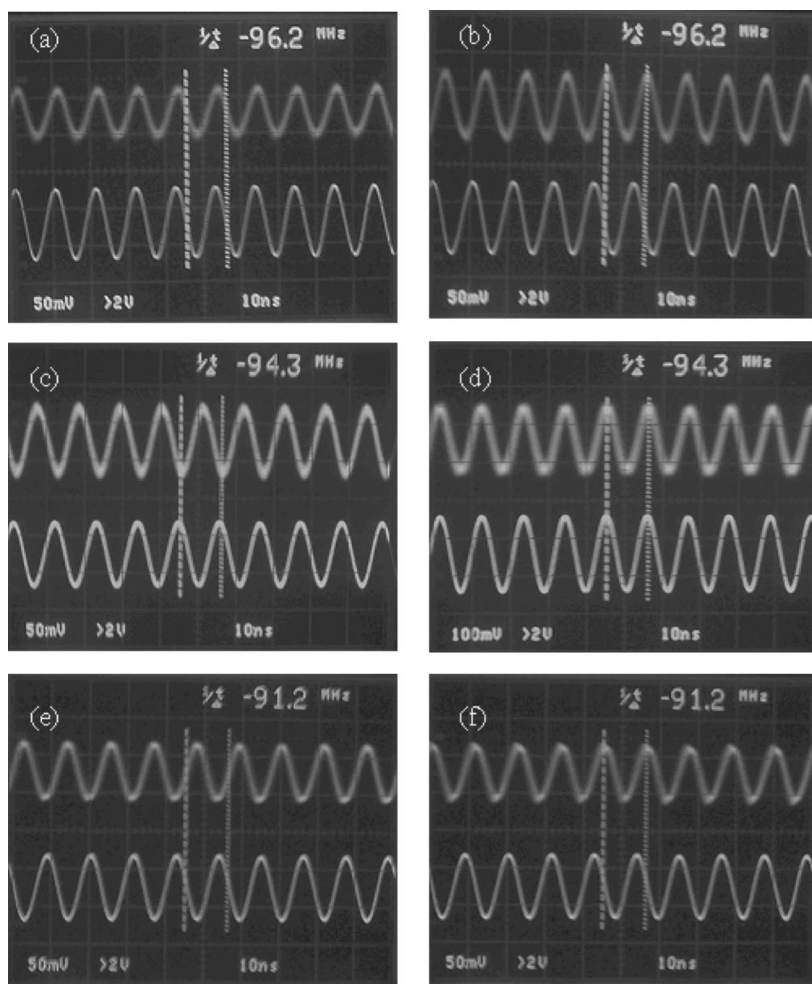


FIG. 10. Instrument provided rf phase shift produced with 1550 nm QWP birefringent sample plug-in plug-out procedure and instrument wavelength tuned to (a, b) 1520 nm @ 96.2 MHz =2 X AOTF drive, (c, d) 1550 nm@ 93.6 MHz=2 X AOTF drive, and (e, f) 1600 nm@ 91.2 MHz=2 X AOTF drive. Top traces from instrument and bottom traces from phase-locked synthesizer. (a,c,e) photos are taken without the QWP inserted and (b,d,f) photos taken with QWP inserted in the instrument.

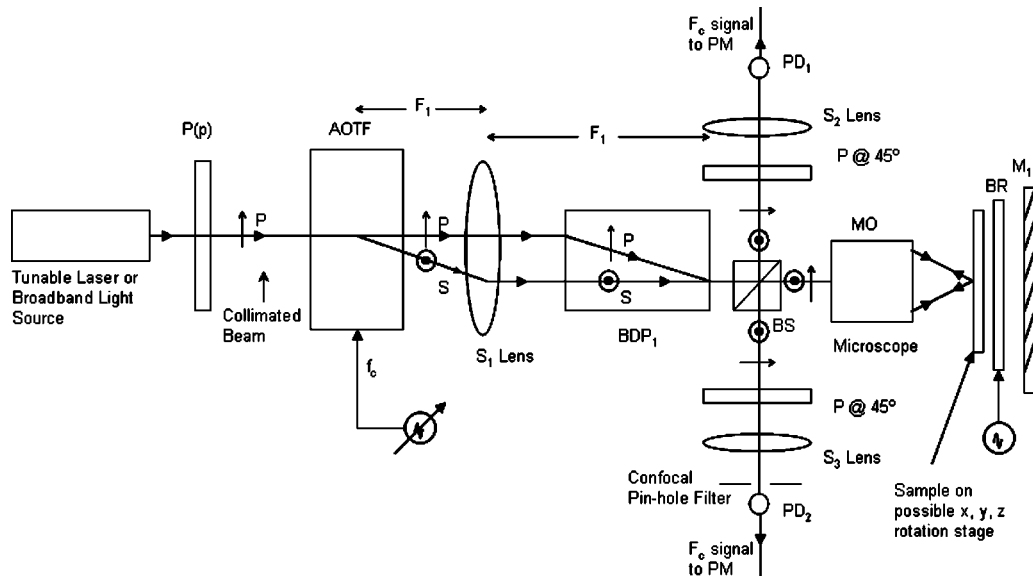


FIG. 11. Proposed alternate spectrally programmable heterodyne optical interferometric confocal microscope design using collinear beams on the sample to enable super high spatial resolution measurements.

the FA and SA are in line with the directions of the polarizations of the two instrument probing beams, i.e., when  $\psi$  is zero or  $90^\circ$ . Note that special cases occur when a QWP or multiple QWPs are used as a test sample. In particular it can be seen in Fig. 3 that for these cases at the rotation angle of  $45^\circ \pm 90^\circ$ , the rf phase shift instantaneously changes by twice the retardation value of the sample. Figure 4 shows that at this  $45^\circ \pm 90^\circ$  FA rotation angle, there is a minimum in the rf amplitude for the QWP case and the signal even drops to zero while for the half wave plate (HWP) case the rf amplitude stays constant. This aspect is experimentally verified in the proposed instrument using a QWP and a HWP for 1550 nm. Note that this rf amplitude modulation behavior based on the position of the sample FA/SA is because of the angle and polarization sensitive anisotropic Bragg diffraction of the AOTF. Specifically, the AOTF diffracts light anisotropically only when the beam polarization and Bragg angle is correct. For example, for the case of the QWP with rotation angle of  $45^\circ \pm 90^\circ$ , the returning light beams to the AOTF have their linear polarizations flipped and hence no longer satisfy the anisotropic Bragg diffraction condition for the AOTF. Hence the off-axis returning  $p$ -polarized beam does not enter the fiber lens. In addition, the returning on-axis (before the AOTF on return path)  $s$ -beam is physically displaced by the birefringent nature of the AOTF and hence does not enter the fiber lens. Hence, for this QWP case with rotation angle of  $45^\circ \pm 90^\circ$ , no returning light can enter the fiber lens and hence the rf signal gets a null. This example indeed shows the vital role of the AOTF for proper operation of the proposed instrument in Fig. 1.

Using the methods discussed in relation to Fig. 3, one can know the orientation of the FA/SA but one cannot say which axis is the FA and which one is the SA. To find out which axis is fast and which is slow in the test material, a programmable bias retarder (BR) is placed between the sample and the mirror in the instrument design as shown in Fig. 1. In Figs. 5 and Fig. 6, this bias retardance effect on the

instrument rf phase and amplitude performance is calculated for the same retardation plates values as in Figs. 3 and 4, but with the BR set for  $(1/10)\pi$  offset retardation. By comparing the rf phase and amplitude change directions in the Fig. 5 and Fig. 6 plots with the Fig. 3 and Fig. 4 plots, respectively, one can access which axis is the FA and which axis is the SA, this completing the material birefringence characterization.

#### IV. DESIGN EXTENSION FOR HIGH RESOLUTION APPLICATIONS

Note that in the Fig. 1 heterodyne microscope design, the two orthogonal linear polarized beams on the sample plane are slightly displaced. This means that for proper birefringence measurements, the physical optical path at the two different locations of the sampling beam pair must be known *a priori* or be the same to detect the birefringence of the sample. In certain cases, this condition for the sample may not be satisfied and hence in this case, both orthogonal polarized beams must occupy the same exact sampling point on the sample. Figure 11 shows the proposed alternate design of the spectrally programmable heterodyne optical interferometric confocal microscope using a polarization beam displacement prism (BDP) to make the two orthogonal linearly polarized beams collocated at the sample plane. The design and operations are similar to mentioned earlier microscope designs, but there are some key modifications. First, after lens  $S1$  a polarizing BDP (e.g., made of Calcite Crystal) is used to combine the two spatially separated  $p$  and  $s$ -beams and thus make them collinear and overlapping at the exit face of the BDP. This polarization beam combining is a unique attribute of the BDP bulk optic that is exploited in the Fig. 11 design. Note that these two beams at the chosen wavelength will have a relative Doppler shift of the AOTF rf drive frequency of  $f_c$ . Both beams after the BDP enter a beamsplitter (BS) that splits the input light power by a de-

sired ratio (e.g., 50:50). Hence, part of the  $p/s$  polarizations beam pair passes to the photodetector PD1 in the reference arm of the microscope. A polarizer oriented at  $45^\circ$  to the  $p$  and  $s$ -directions interferometrically combines the beam pair to produce a reference phase rf signal at  $f_c$  that feeds the reference phase port of a rf power meter (PM). The other part of the beam pair enters a microscope objective (MO) assembly that forms a focused spot (i.e., two spots overlapping each other but of  $p$  and  $s$  polarizations) on the sample under observation. The sample can be naturally reflective (e.g., human eye) or placed in a holder that contains the bias retarder (BR) and mirror  $M1$ . The sample assembly reflected light now containing the sample birefringence information for the chosen wavelength returns to the BS via the MO and is directed to the signal path photodetector PD2 that generates the rf signal  $f_c$  with the correct sample rf phase. Again, a polarizer at  $45^\circ$  to the  $p$  and  $s$  directions is used to produce the desired interference signal. Optional lenses  $S2$  and  $S3$  can be used to collect the light efficiently onto the high speed photodetectors. The signal and reference rf signals at frequency  $f_c$  are fed to a rf phase meter that provides both signal amplitude and phase information that gives the sample localized reflectance and birefringence for a given chosen wavelength. Recall that the wavelength is either chosen by tuning the laser and matching the correct AOTF rf drive or using a broadband source and then selecting the correct AOTF rf to select the desired wavelength for optical heterodyne interferometry. Note that the sample can be placed on a rotation,  $x, y, z$  motion stage to implement three-dimensional (3D) confocal scanning microscopy when used in conjunction with a pinhole filter placed near PD2. Thus a 3D scanning high spatial resolution heterodyne confocal spectral microscope is formed. Do note that instead of using a single AOTF and one BDP, the dual-beam generation method can be formed using two cascaded AO devices<sup>13,14</sup> to form a spectrally programmable heterodyne optical interferometric confocal microscope with more flexibility in rf selection.

## V. DISCUSSION

Appropriate large aperture microscope focusing optics can be used between the AOTF and the test sample to form a

high spatial resolution (e.g., 1.5 microns diameter) beam. Because both tunable lasers and AOTFs can be tuned at high speeds (ms to ns), fast spectral information about the sample material can be obtained creating high resolution spatial and volumetric maps. By using a much shorter lens  $S$ , the  $0.5^\circ$  rf phase measurement stability of the instrument can be improved. In addition, using a shorter focal length  $S$  decreases the separation between the two sample probing beams, thus allowing more localized birefringence measurements. High speed tuning of the laser along with no-moving parts high speed (e.g., microseconds) spectral filtering/tuning via the AOTF give powerful new spectral processing attributes for the proposed instrument such as implementation of high speed FT OCT or Two photon fluorescence microscopy. Future work relates to design optimization of the instrument to improve measurement stability, operational optical bandwidth, sample scan zone using frontend scan optics, and package size.

## ACKNOWLEDGMENTS

The authors would like to thank Professor J. Wolter from the Technical University of Eindhoven, Netherlands for suggesting project work for M. Bakker with Dr. Riza. Thanks also to Dr. Frank Perez at Nuonics, Inc. for his original technical and design contributions and AOTF device support. Support from J. Kump at Crystal Tech., CA is also appreciated.

<sup>1</sup>G. Birnbaum, E. Cory, and K. Gow, Appl. Opt. **13**, 1660 (1974).

<sup>2</sup>S. R. M. Robertson, Appl. Opt. **22**, 2213 (1983).

<sup>3</sup>J. R. Mackey, Meas. Sci. Technol. **10**, 946 (1999).

<sup>4</sup>B. Wang and T. C. Oakberg, Rev. Sci. Instrum. **70**, 3847 (1999).

<sup>5</sup>X. D. Xu, S. Y. Zhang, and P. K. Kuob, Rev. Sci. Instrum. **74**, 639 (2003).

<sup>6</sup>M. Raab and A. Weber, J. Opt. Soc. Am. B **2**, 1476 (1985).

<sup>7</sup>M. G. Shlyagin, A. V. Khomenko, and D. Tentori, Opt. Lett. **20**, 869 (1995).

<sup>8</sup>T. Fukano and I. Yamaguchi, Opt. Lett. **25**, 548 (2000).

<sup>9</sup>Yuuki Watanabe and Ichirou Yamaguchi, Appl. Opt. **41**, 2414 (2002).

<sup>10</sup>N. A. Riza and M. A. Arain, Appl. Opt. **42**, 2341 (2003).

<sup>11</sup>N. A. Riza, F. Perez, and A. Bokhari, U.S. Patent Pending.

<sup>12</sup>M. V. Buren and N. A. Riza, Appl. Opt. **42**, 550 (2003).

<sup>13</sup>N. A. Riza, U.S. Patent No. 5 694 216 (1997).

<sup>14</sup>N. A. Riza, Rev. Sci. Instrum. **67**, 2466 (1996).